Research Article Vol. 10, No. 7 / July 2022 / Photonics Research 1567

PHOTONICS Research

Sn content gradient GeSn with strain controlled for high performance GeSn mid-infrared photodetectors

Xiangquan Liu,[1,2] Jun Zheng,[1,2,*] Chaoqun Niu,[1,2] Taoran Liu,[1,2] Qinxing Huang,[1,2] Mingming Li,[1,2] Diandian Zhang,[1,2] Yaqing Pang,[1,2] Zhi Liu,[1,2] Yuhua Zuo,[1,2] and Buwen Cheng[1,2]

[1]State Key Laboratory on Integrated Optoelectronics, Institute of Semiconductors, Chinese Academy of Sciences, Beijing 100083, China
[2]Center of Materials Science and Optoelectronics Engineering, University of Chinese Academy of Sciences, Beijing 100049, China
*Corresponding author: zhengjun@semi.ac.cn

Received 10 February 2022; revised 17 May 2022; accepted 17 May 2022; posted 17 May 2022 (Doc. ID 456000); published 10 June 2022

GeSn detectors have attracted a lot of attention for mid-infrared Si photonics, due to their compatibility with Si complementary metal oxide semiconductor technology. The GeSn bandgap can be affected by Sn composition and strain, which determines the working wavelength range of detectors. Applying the Sn content gradient GeSn layer structure, the strain of GeSn can be controlled from fully strained to completely relaxed. In this work, the strain evolution of GeSn alloys was investigated, and the effectiveness of gradually increasing Sn composition for the growth of high-Sn-content GeSn alloys was revealed. Relaxed GeSn thick films with Sn composition up to 16.3% were grown, and GeSn photodetectors were fabricated. At 77 K, the photodetectors showed a cutoff wavelength up to 4.2 μm and a peak responsivity of 0.35 A/W under 1 V at 2.53 μm. These results indicate that GeSn alloys grown on a Sn content gradient GeSn structure have promising application in mid-infrared detection. © 2022 Chinese Laser Press

https://doi.org/10.1364/PRJ.456000

1. INTRODUCTION

Mid-infrared (MIR) has important applications in medicine, gas detection, and pollution monitoring, due to the strong absorption in this wavelength range. At present, the materials used for fabricating MIR detectors are expensive semiconductors, such as HgCdTe, PbS, and antimonide-based type II superlattice [1–4]. The high manufacturing cost and difficulty in integrating photons and electrons on a single wafer hinder the wide application of MIR photonics. Combining the features of mass production and compatibility of complementary metal oxide semiconductor (CMOS) technology with optoelectronic technology, Si photonics has achieved great success in the near-infrared (NIR) field and is also considered to be a promising solution for MIR photonics [5–8]. Recently, Si-based passive photonic components operated at MIR, such as couplers, waveguides, and filters, have been designed and fabricated [9–11]. As group IV material, $Ge_{1-x}Sn_x$ alloys are considered to be an ideal choice for making active photonic components due to their tunable bandgap energy from 0.66 to 0 eV, covering the whole MIR field [12–15]. By increasing Sn composition, the detection range of GeSn devices reported in literature has extended from short-wave infrared (SWIR) to the MIR region in the last decade [16–22].

However, GeSn alloys with high Sn composition and high crystal quality are difficult to grow because of the large lattice mismatch between Ge and α-Sn, low-equilibrium solid solubility (<1%) of Sn in Ge, and easy Sn segregation at high temperature [23–26]. Several epitaxial techniques, such as chemical vapor deposition (CVD) [12,13], molecular beam epitaxy (MBE) [14,15,23], and sputtering epitaxy [24–26] have been developed to grow GeSn alloys. It is reported that a spontaneous-relaxation-enhanced (SRE) Sn incorporation mechanism during epitaxy by CVD can help to grow relaxed GeSn alloys with high Sn content and low threading defect density, and GeSn optoelectronic devices have been fabricated with good performance [21,27–29]. However, for GeSn grown by physical vapor deposition (PVD) methods, the GeSn relaxation process with high Sn composition always has a large number of dislocations, and no spontaneous Sn composition gradient phenomenon is observed [14,23]. In previous work, it was found that the strain of GeSn alloys was released effectively by designing a Sn component gradient GeSn buffer layer by sputtering epitaxy [30]. For the MBE system, Sn content is regulated by controlling the temperature of the pyrolytic boron nitride (BN) crucible, and the Sn content of GeSn alloys can increase more slowly along the thickness. This suggests that relaxed GeSn

2327-9125/22/071567-08 Journal © 2022 Chinese Laser Press

alloys with improved crystal quality can be achieved by MBE using a Sn content gradient GeSn buffer layer structure.

In this work, an effective method of gradually increasing Sn composition for growing high-Sn-content GeSn alloys is proposed. Fully relaxed $Ge_{0.837}Sn_{0.163}$ alloys without Sn segregation are realized by MBE. The structural and bandgap properties of Sn fraction graded GeSn alloys are investigated in detail. GeSn photodetectors are fabricated with a cutoff wavelength up to 4.2 μm at 77 K. The results indicate that GeSn alloys with high Sn content can be grown by MBE, and GeSn photodetectors have promising applications in the development of MIR Si photonics.

2. EXPERIMENT

A. Material Growth and Characterization

GeSn samples were grown by MBE on 4-inch n-type Ge (100) substrates. After transferring into a growth chamber with a base pressure of less than 1×10^{-7} Pa, the Ge substrates were heated to 400°C to grow a 50 nm Ge buffer by thermally evaporating the Ge in the pyrolytic BN crucible. Then, after the substrates were cooled to the growth temperature (150°C–170°C), four GeSn samples were deposited by evaporating Ge and Sn at the same time. The deposition rate of GeSn is about 0.036 nm/s. To release the compressive strain, Sn composition graded GeSn buffers are designed, which is achieved by fixing the temperature of the Ge crucible at 1300°C and linearly increasing the temperature of the Sn crucible. The growth conditions are listed in Table 1. For samples A, B, and C, the initial temperature of the Sn crucible is 760°C, and the final temperature is gradually increased. For sample D, when the Sn crucible reaches 835°C, the GeSn layer continues to grow for about 200 nm with the Sn crucible temperature unchanged. The Sn composition was determined by secondary ions mass spectrometry (SIMS), and degree of strain relaxation (R) was calculated using reciprocal space mapping (RSM). Atomic force microscopy (AFM), scanning electron microscopy (SEM), and cross-sectional transmission electron microscopy (XTEM) were utilized to investigate the surface morphology and crystal quality.

Table 1. Summary of Growth Temperature (T_{growth}), Sn Crucible Temperature (T_{Sn}), Measured Sn Content (x), and Root Mean Square (RMS) Roughness of GeSn Samples[a]

Samples	T_{growth} (°C)	T_{Sn} (°C)	x (%)	RMS (nm)
A	170	760–820	2.2–8.6 (I) 8.6–11.2 (II)	1.60
B	150	760–835	2.0–7.0 (I) 7.0–8.9 (II) 8.9–14.2 (III)	0.90
C	150	760–850	2.0–7.3 (I) 7.3–8.7 (II) 8.7–20.3 (III)	1.32
D	150	760–835	2.0–7.1 (I) 7.1–8.7 (II) 8.7–16.3 (III)	2.04

[a]I is the Sn composition range with R of 0%, II is the Sn composition range with R of 0% to 100%, and III is the Sn composition range with R of 100%.

B. Device Fabrication and Characterization

GeSn photodetectors with an interdigital electrode structure were fabricated by CMOS compatible technology. First, the rectangular mesa of GeSn was defined and etched by photolithography and inductively coupled plasma (ICP) equipment. Subsequently, 300 nm thick SiO_2 was deposited by plasma enhanced CVD (PECVD) to passivate the etched GeSn sidewall. After etching to form metal contact holes, the Ni/Al electrode was deposited and patterned by lift-off. The width and spacing of the interdigital electrodes were 5 and 20 μm, respectively. The dark current–voltage (I – V) curves at different temperatures were measured by a low-temperature probe station and a semiconductor parameter analyzer. Spectral-response measurements at different temperatures were performed by a Nicolet 6700 Fourier transform infrared spectrometer (FTIR). The photodetectors were placed in a liquid-nitrogen cryostat equipped with a ZnSe window for temperature regulation. The photocurrent signal was amplified by a current amplifier, and the photocurrent spectra were obtained finally.

3. RESULTS AND DISCUSSION

A. Materials Research

A schematic diagram of epitaxial structure of GeSn alloys with gradually increasing Sn composition is shown in the inset of Fig. 1(a). To explore the Sn composition and strain state of GeSn samples, RSM measurements were carried out, and the results are shown in Fig. 1. Moreover, the Sn composition is also obtained by SIMS, shown later in Fig. 4. The in-plane and out-of-plane lattice parameters ($a_{\parallel}$ and $a_{\perp}$) are obtained from (Q_x, Q_z) coordinates of (−2 −2 4) RSM, and then the Sn composition and R are calculated [14,30]. The diffraction regions in RSM were divided into three parts: I, II, and III. Diffraction region I has the same Q_x value as a Ge substrate (same $a_{\parallel}$ value), indicating that GeSn alloys in this region are fully strained ($R = 0\%$). Then, as the Sn composition increases, the strain state of diffraction region II gradually approaches the relaxation line ($0\% < R < 100\%$), and finally reaches fully relaxed diffraction region III ($R = 100\%$). The distribution of Sn content in three diffraction regions of GeSn samples is listed in Table 1. It is worth noting that sample A shows only regions I and II; even if the Sn composition is up to 11.2%, while other samples appear in region III once the Sn content reaches about 9%. Furthermore, it can be observed that, compared with other GeSn samples, the threshold Sn composition for region II is about 8.6% for sample A and is decreased to about 7% for other samples. This indicates that it is easier for GeSn alloys to relax at a low growth temperature. This is mainly because a high growth temperature can facilitate atoms to migrate to the appropriate position easily, and the accumulated stress is released by surface fluctuations rather than creating relaxation-favorable dislocations. Therefore, a larger lattice mismatch (higher Sn composition) is required for starting relaxation at a high growth temperature. After GeSn alloys are fully relaxed ($R = 100\%$), the Sn composition can be further increased. For samples B and C, the highest Sn composition of the fully relaxed GeSn alloys reaches 14.2% and 20.3%, respectively. No Sn segregation is observed for sample B, while some Sn segregation clusters appear for sample C [inset of

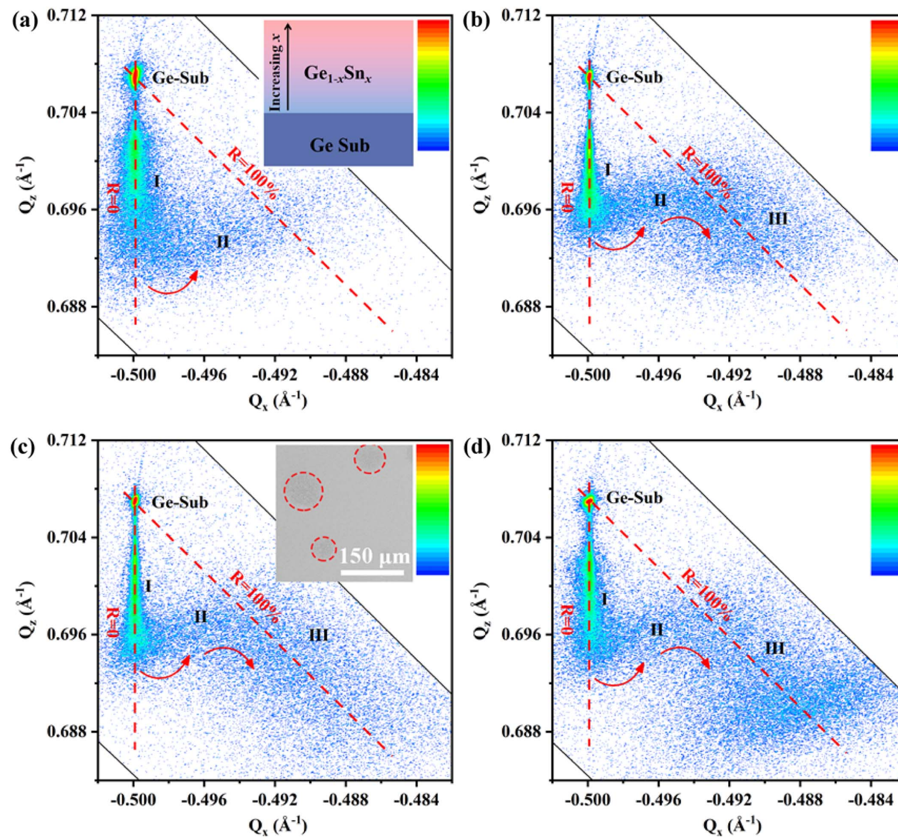

Fig. 1. RSM around the asymmetric (−2 −2 4) reflection of (a) sample A; (b) sample B; (c) sample C; (d) sample D. The inset of (a) shows an schematic diagram of epitaxial structure of GeSn alloy. The inset of (c) shows an SEM image of sample C, and the positions marked by the red circle are the segregated Sn.

Fig. 1(c)]. This is likely because the growth temperature is still too high for growing GeSn film with Sn content around 20%.

To prove the assumption that the thick GeSn film can still be grown on the relaxed GeSn layer, sample D was prepared with the top GeSn layer thickness of about 200 nm on the same Sn composition gradient layer as sample B. As shown in Fig. 1(d), the top GeSn layer of sample D is fully relaxed, and its Sn composition reaches 16.3%. Sn segregation does not happen in sample D. This indicates that a thick and high-Sn-content GeSn layer can be grown on the relaxed buffer layer.

To confirm the Sn composition and strain state of GeSn samples obtained from RSM, Raman scattering measurements were also performed using a 488 nm incident laser (penetration depth is less than 20 nm in GeSn alloys). For fully relaxed GeSn alloys, the Raman shift of the Ge-Ge longitudinal optical (LO) peak ($\omega_{\text{Ge-Ge}}$) can be written as $\omega_{\text{Ge-Ge}} = \omega_0 + ax$, where x is the Sn composition, and $\omega_0 = 301\ \text{cm}^{-1}$ and $a = -78\ \text{cm}^{-1}$ are the bulk Ge Raman frequency and Raman Sn content coefficient, respectively [31]. The top Sn composition measured by RSM is used to predict the $\omega_{\text{Ge-Ge}}$ of GeSn samples. As shown in Fig. 2, calculated and measured $\omega_{\text{Ge-Ge}}$ are consistent, which proves the accuracy of the results obtained by RSM.

XTEM tests were conducted to reveal the strain relaxation mechanism in the film. Figure 3(a) shows XTEM images of sample D. No obvious threading defects are observed, and stress fringes appear at the low-Sn-content layer (about 200 nm). The inset of Fig. 3(a) shows energy dispersive X-ray spectroscopy (EDX) Ge and Sn element mapping. The closer to the surface, the more obvious the red color, which directly indicates the increase in Sn composition in GeSn alloys. The top GeSn alloy has uniform Sn composition, and the Sn content is about 16.5% from EDX. Figure 3(b) shows a high-resolution XTEM image of GeSn alloys at the bottom and its fast Fourier

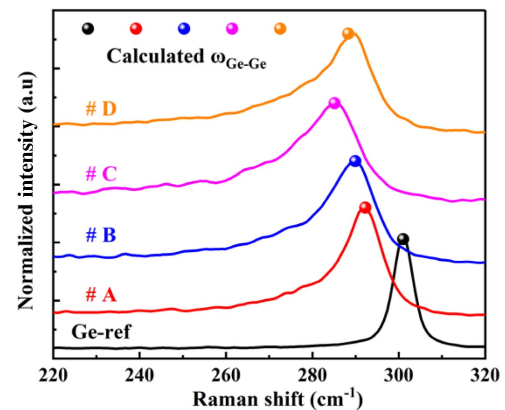

Fig. 2. Raman scattering spectra of GeSn samples and a Ge wafer for reference, and the position of the ball corresponds to the calculated Ge-Ge Raman shift.

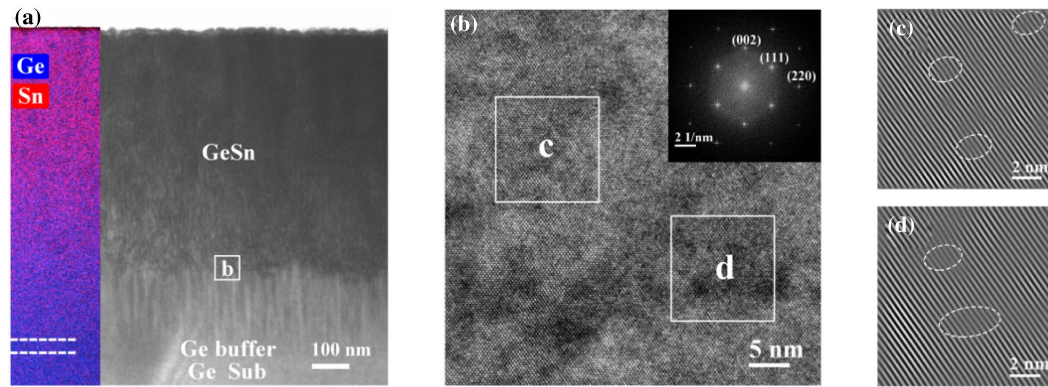

Fig. 3. (a) Full view of XTEM image of sample D; inset: EDX Ge and Sn element mapping. (b) High-resolution XTEM image and FFT pattern of area "b" in (a). (c), (d) Inverse FFT images of the rectangular area in (b).

transform (FFT) pattern. The clear lattice fringes and typical diffraction pattern evidence the single crystalline layer. It is worth noting that there are some point defects in the GeSn alloys, which can be spotted in the inverse FFT images of Figs. 3(c) and 3(d). The existence of defects makes the lattice arrangement discontinuous and can release the stress caused by the large lattice mismatch.

Figure 4 demonstrates the SIMS and bandgap calculations of four samples. As expected, the Sn composition is increased gradually along the thickness, which is consistent with the RSM results discussed above. The three region colors are used to represent fully strained, partially relaxed, and fully relaxed states, according to the RSM measurements. From Fig. 4, the rate of Sn composition increase can be divided into the three parts. At the initial growth, the slope of Sn composition increase is about 3.4%/100 nm and changes to about 1.1%/100 nm in the fully strained state. After the sample becomes fully relaxed, the slope of Sn composition increase is enhanced to about 2.5%/100 nm. This indicates that relaxing the strain in the GeSn film can help to incorporate more Sn atoms into the film, which is also observed in GeSn film grown by CVD. As shown in Fig. 4, the thickness of region II (partially relaxed state) for sample A is >70 nm, but only about 50 nm for samples B, C, and D. Thus, low growth temperature can lead to fast relaxation for GeSn heterogeneous growth. Once entering partial relaxation, the slope of Sn composition increases greatly, reaching 3.9%/100 nm. This fast relaxation process does not introduce threading dislocations but point defects, as revealed by XTEM results. By further optimizing the growth condition of the region II layer, the defects caused by the lattice mismatch can be confined in this layer, providing a high-quality buffer layer for subsequent GeSn growth.

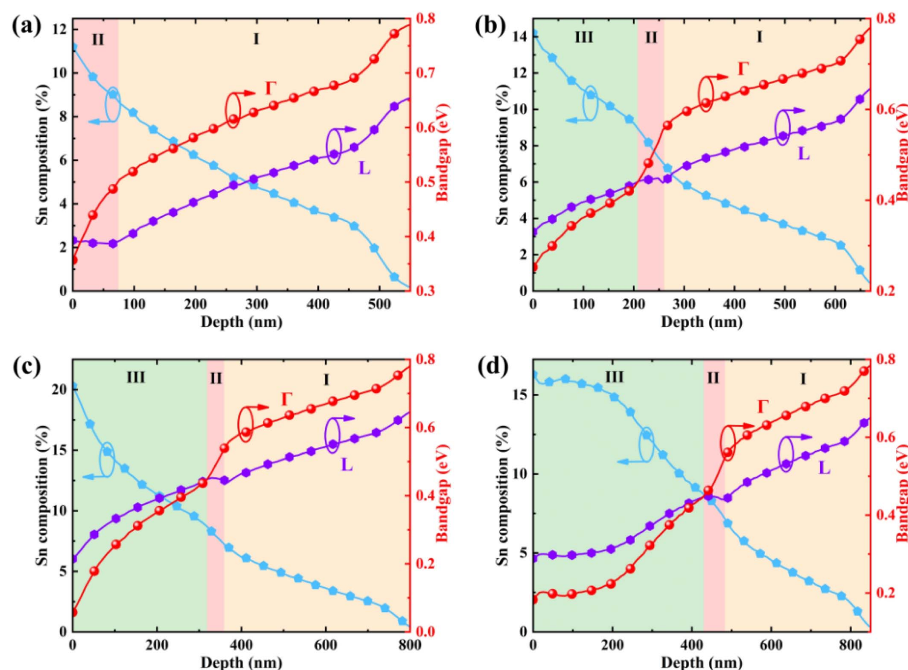

Fig. 4. SIMS profile of Sn composition and bandgap calculations at different depths of (a) sample A; (b) sample B; (c) sample C; (d) sample D. Regions marked with different colors correspond to different strain states of the RSM in Fig. 1.

The direct bandgap (E^Γ) and indirect bandgap (E^L) are calculated based on the Sn composition and strain state obtained by SIMS and RSM, respectively [32]. For fully relaxed $Ge_{1-x}Sn_x$ alloys, E^Γ and E^L can be expressed as $E(Ge_{1-x}Sn_x) = E_{Ge}(1-x) + E_{Sn}x - bx(1-x)$, where E_{Ge} and E_{Sn} are the bandgaps of Γ or L valleys for Ge and α-Sn, respectively; b is the bowing parameter. The strain in GeSn alloys will shift the band edges of the conduction band (CB) and valence band (VB), which can be written as $\Delta E_c = a_c(\varepsilon_{xx} + \varepsilon_{yy} + \varepsilon_{zz})$ and $\Delta E_v = b_v(\varepsilon_{xx} + \varepsilon_{yy} + \varepsilon_{zz}) + b_s(\varepsilon_{zz} - \varepsilon_{xx})$, where ε_{xx} and ε_{yy} are the in-plane strains, ε_{zz} is the out-of-plane strain, a_c is the CB deformation potential, and b_v and b_s are the VB deformation potentials. The bandgaps of GeSn alloys are the combined effect of Sn composition and strain. In region I, the energy difference of Γ and L valleys ($\Delta_{\Gamma L} = E^\Gamma - E^L$) is almost kept the same with increasing Sn content, and GeSn film is still indirect bandgap material because of the fully strained state. For region II, the decreasing rate of E^Γ is obviously faster than that of E^L. Finally, the $\Delta_{\Gamma L}$ values are less than zero, indicating that the GeSn films become direct bandgap materials. Thus, strain relaxation can not only incorporate more Sn atoms into the film [13], but also help the transformation of the direct bandgap. For region III, as the Sn content along the thickness continues to increase, the $\Delta_{\Gamma L}$ values decrease more. For samples A, B, C, and D, the E^Γ of the top GeSn layer reaches 0.36, 0.25, 0.06, and 0.18 eV, respectively, suggesting the potential application of GeSn materials for fabricating MIR detectors.

For GeSn films with high Sn content, Sn segregation may easily happen during growth. To investigate the Sn segregation phenomenon in the as-grown Sn gradient GeSn samples, AFM and SEM measurements were performed. The root mean square (RMS) roughness of the GeSn samples is listed in Table 1. The RMS results show that high growth temperature and high Sn composition can cause surface undulations. Moreover, the GeSn layer can maintain its crystal quality by increasing the layer thickness if the GeSn layer is relaxed without Sn segregation. From the SEM results, it is found that only sample C has Sn segregation in some areas [inset of Fig. 1(c)] due to the relatively high Sn content. By decreasing the growth temperature, Sn segregation can also be avoided. Compared with other PVD-grown GeSn work [15,23], the direct growth of GeSn alloys with high Sn composition will generate a large number of threading dislocations, and the Sn surface segregation is severe. The Sn composition graded structure can effectively avoid these problems, which is helpful in growing GeSn alloys with high Sn composition.

So far, relaxed GeSn alloys with high Sn composition were mainly achieved by CVD. The characterization of GeSn materials in this work shows that it is feasible to grow high-Sn-content GeSn films by MBE through applying GeSn buffer layers with gradually increasing Sn content. The thickness of relaxed GeSn alloys with high Sn content can also be further increased on the Sn gradient GeSn structure, which lays the foundation for the preparation of high-performance MIR GeSn devices.

B. Photodetector Analysis

To study the photoelectric performance of the Sn content gradient GeSn film, sample D was used to fabricate a GeSn photodetector. The photodetector has an interdigital electrode structure, and a three-dimensional schematic and top view are shown in Fig. 5(a). As shown in Fig. 5(b), the anode and cath-

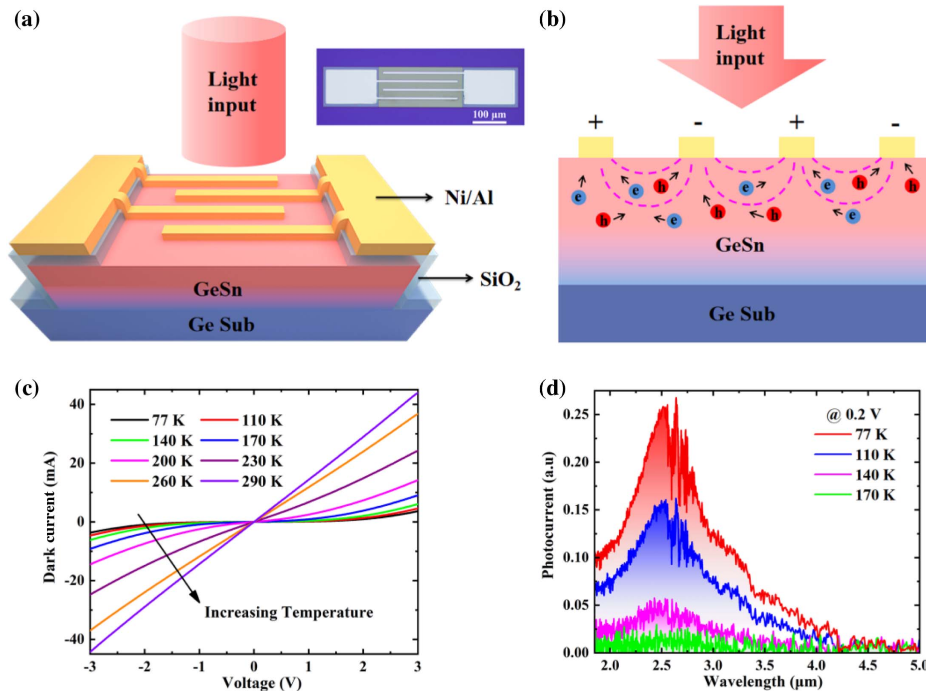

Fig. 5. (a) Three-dimensional schematic of GeSn photodetector with interdigital electrode structure. The inset shows the top view of the device. (b) Working mechanism of GeSn photodetector under light incident conditions. (c) Dark $I-V$ curves of GeSn photodetector at different temperatures. (d) Photocurrent spectra of the GeSn photodetector at 0.2 V for different temperatures.

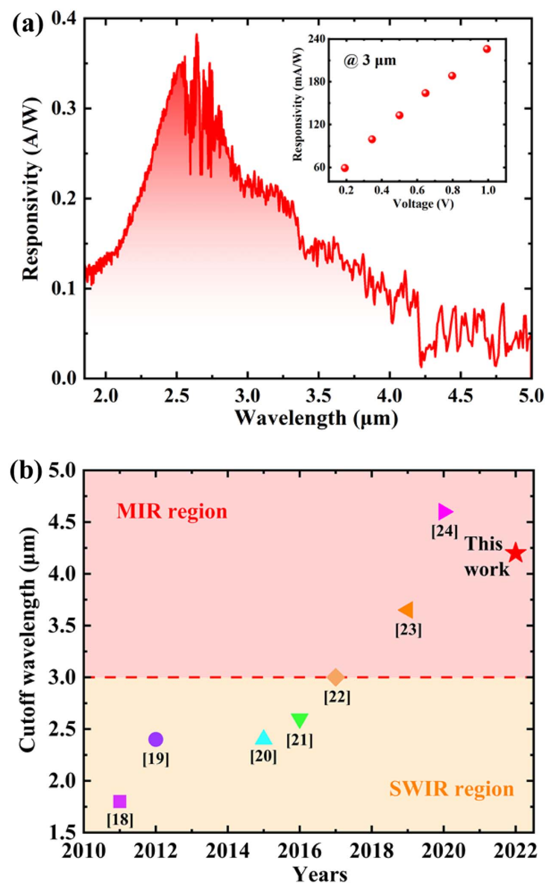

Fig. 6. (a) Wavelength-dependent optical responsivity of GeSn photodetector under a bias voltage of 1 V at 77 K. Inset: responsivity at 3 μm as a function of voltage at 77 K. (b) Comparison of cutoff wavelength of GeSn photodetectors in different works.

ode electrodes are distributed at intervals, forming the electric field points from the anode to cathode when applying voltage. Under light incident conditions, photo-generated carriers are formed in the VB and CB, which are collected by the nearby anode and cathode electrodes. Figure 5(c) shows the symmetrical dark $I-V$ curves of the GeSn photodetector at different temperatures. The electrode contact is a Schottky contact at low temperature (<230 K). At 77 K, the dark currents are 0.13 and 3.64 mA under 1 and 3 V, respectively. As the temperature increases, more carriers are thermally activated to cross the barrier. Compared with those measured at 77 K, the dark current at 290 K increases by factors of about 110 and 12 under 1 and 3 V, respectively.

Figure 5(d) shows the photocurrent spectra of the GeSn photodetector at 0.2 V for different temperatures. With the increase in temperature, the defects acting as a non-radiative center can be activated, which would lead to a decrease in optical response. Moreover, the intrinsic carrier concentration is also increased as the temperature increases. These can lead to a decrease in the signal-to-noise ratio, and GeSn photodetectors work better in cooling conditions. The signal distortion from 2.58 to 2.77 μm, sudden decrease near 3.36 μm, and jitter around 4.2–4.3 μm are attributed to the absorption of carbon dioxide and water. At 77 K, the cutoff wavelength of the photodetector can reach about 4.2 μm, which is defined based on the intensity decay to 10%. Using a blackbody light source, the intensity value of the photocurrent was tested, and the responsivity of the detector was calibrated. Figure 6(a) shows the wavelength-dependent optical responsivity of the GeSn photodetector under a bias voltage of 1 V at 77 K. The peak wavelength is near 2.53 μm, and its responsivity is about 0.35 A/W. In addition, as the bias voltage increases, the responsivity increases linearly, as shown in the inset of Fig. 6(a). Under a bias voltage of 1 V, the responsivity at 3 μm is up to 226 mA/W.

Specific detectivity (D^*) can represent the sensitivity performance of a detector, and D^* is estimated according to $D^* = R_i/(2eI_{\text{dark}}/A)^{1/2}$, where R_i is the responsivity at a specific incident wavelength, e is the elementary charge, I_{dark} is the dark current, and A is the effective area of the photodetector [6,33]. For $Ge_{0.837}Sn_{0.163}$ photodetectors, peak D^* is about 9.3×10^8 cm Hz$^{1/2}$ W^{-1} at 1 V and 77 K. As listed in Table 2, peak D^* decreases with increasing Sn composition and ranges from 10^8 to 10^{10} cm Hz$^{1/2}$ W^{-1} for $Ge_{1-x}Sn_x$ ($10\% < x < 20\%$) detectors. By optimizing the structure of a GeSn photoconductive detector, the performance can be further improved in the future.

Figure 6(b) shows a comparison of cutoff wavelength of GeSn photodetectors in different works. The detailed performance parameters of GeSn photodetectors are also listed in Table 2. With the development of GeSn material epitaxy technology, the Sn composition in GeSn photodetectors increases, and the cutoff wavelength extends to the MIR (>3 μm). The cutoff wavelength shown in this work is very long among the reported GeSn photodetectors [16–22]. This confirms that

Table 2. Summary of the Performance of GeSn Photodetectors[a]

Reference	Sn Content	Structure	Epitaxial Technique	Peak Specific Detectivity (cm Hz$^{1/2}$ W^{-1})	Responsivity (A/W)	Cutoff Wavelength (μm)
[16]	3%	PIN	MBE	–	0.12 at 1.64 μm at −1 V at RT	1.8 μm
[17]	9%	QW/PC	CVD	–	0.1 at 2.2 μm at 5 V at RT	2.4 μm
[18]	10%	PC	CVD	~4.6×10^9 at 77 K	1.63 at 1.55 μm at 50 V at 77 K	2.4 μm
[19]	10%	PIN	CVD	2.4×10^9 at 77 K	0.19 at 1.55 μm at − 0.1 V at RT	2.6 μm
[20]	11%	PC	CVD	2.0×10^{10} at 77 K	28.5 at 1.55 μm at 2 V at 77 K	3.0 μm
[21]	20%	PC	CVD	1.1×10^8 at 77 K	0.8 at 2.0 μm at 5 V at 77 K	3.65 μm
[22]	17%	PC	CVD	–	0.004 at 2.4 μm at ~1 V at RT	4.6 μm
This work	**16.3%**	**PC**	**MBE**	**9.33×10^8 at 77 K**	**0.35 at 2.53 μm at 1 V at 77 K**	**4.2 μm**

[a] PC is the photoconductor of MSM structure, and PIN is the photodiode of p-i-n structure.

GeSn alloys with high Sn content can be grown by MBE using a Sn composition gradient structure. The long cutoff wavelength makes GeSn more competitive in the field of infrared detection, and is expected to play an important role in gas sensing, environmental monitoring, and so on.

4. CONCLUSION

Strain-controlled GeSn films were proposed using the method of gradually increasing Sn content along the growth thickness. The Sn composition, strain state, and crystal quality were investigated in detail by RSM, SIMS, and XTEM. At the initial growth, the GeSn alloys were fully strained, and then relaxed rapidly as the Sn composition increased. After the full relaxation process, the Sn content and thickness of GeSn alloys can be further increased without Sn segregation. The $Ge_{0.837}Sn_{0.163}$ photodetectors were fabricated with a cutoff wavelength of about 4.2 μm. At 77 K, the peak responsivity was about 0.35 A/W under a bias voltage of 1 V at 2.53 μm. These results show that GeSn photodetectors have promising applications in MIR Si photonics.

Funding. National Key Research and Development Program of China (2018YFB2200500); National Natural Science Foundation of China (61975196, 62050073, 62090054); Key Research Program of Frontier Science, Chinese Academy of Sciences (QYZDY-SSW-JSC022).

Disclosures. The authors declare no conflicts of interest.

Data Availability. Data underlying the results presented in this paper are not publicly available at this time but may be obtained from the authors upon reasonable request.

REFERENCES

1. A. Rogalski, "HgCdTe infrared detector material: history, status and outlook," Rep. Prog. Phys. **68**, 2267–2336 (2005).
2. J. P. Clifford, G. Konstantatos, K. W. Johnston, S. Hoogland, L. Levina, and E. H. Sargent, "Fast, sensitive and spectrally tuneable colloidal-quantum-dot photodetectors," Nat. Nanotechnol. **4**, 40–44 (2009).
3. H. S. Kim, "Dark current analysis of an InAs/GaSb type II superlattice infrared photodiode with SiO_2 passivation," J. Korean Phys. Soc. **78**, 1141–1146 (2021).
4. Y. Liu, C. Zhang, X. Wang, J. Wu, and L. Huang, "Interface investigation of InAs/GaSb type II superlattice for long wavelength infrared photodetectors," Infrared Phys. Technol. **113**, 103573 (2021).
5. N. Wang, C. Xue, F. Wan, Y. Zhao, G. Xu, Z. Liu, J. Zheng, Y. Zuo, B. Cheng, and Q. Wang, "High-performance GeSn photodetector covering all telecommunication bands," IEEE Photon. J. **13**, 6800809 (2021).
6. F. Yang, K. Yu, H. Cong, C. Xue, B. Cheng, N. Wang, L. Zhou, Z. Liu, and Q. Wang, "Highly enhanced SWIR image sensors based on $Ge_{1-x}Sn_x$-graphene heterostructure photodetector," ACS Photon. **6**, 1199–1206 (2019).
7. H. Cong, C. L. Xue, J. Zheng, F. Yang, K. Yu, Z. Liu, X. Zhang, B. W. Cheng, and Q. M. Wang, "Silicon based GeSn p-i-n photodetector for SWIR detection," IEEE Photon. J. **8**, 6804706 (2016).
8. X. Li, L. Peng, Z. Liu, Z. Zhou, J. Zheng, C. Xue, Y. Zuo, B. Chen, and B. Cheng, "30 GHz GeSn photodetector on SOI substrate for 2 μm wavelength application," Photon. Res. **9**, 494–500 (2021).
9. M. Nedeljkovic, J. S. Penades, C. J. Mitchell, A. Z. Khokhar, S. Stankovic, T. D. Bucio, C. G. Littlejohns, F. Y. Gardes, and G. Z. Mashanovich, "Surface-grating-coupled low-loss Ge-on-Si rib waveguides and multimode interferometers," IEEE Photon. Technol. Lett. **27**, 1040–1043 (2015).
10. L. Shen, N. Healy, C. J. Mitchell, J. S. Penades, M. Nedeljkovic, G. Z. Mashanovich, and A. C. Peacock, "Mid-infrared all-optical modulation in low-loss germanium-on-silicon waveguides," Opt. Lett. **40**, 268–271 (2015).
11. T. Hu, B. Dong, X. Luo, T.-Y. Liow, J. Song, C. Lee, and G.-Q. Lo, "Silicon photonic platforms for mid-infrared applications," Photon. Res. **5**, 417–430 (2017).
12. S. Assali, J. Nicolas, and O. Moutanabbir, "Enhanced Sn incorporation in GeSn epitaxial semiconductors via strain relaxation," J. Appl. Phys. **125**, 025304 (2019).
13. W. Dou, M. Benamara, A. Mosleh, J. Margetis, P. Grant, Y. Zhou, S. Al-Kabi, W. Du, J. Tolle, B. Li, M. Mortazavi, and S. Q. Yu, "Investigation of GeSn strain relaxation and spontaneous composition gradient for low-defect and high-Sn Alloy growth," Sci. Rep. **8**, 5640 (2018).
14. F. Wan, C. Xu, X. Wang, G. Xu, B. Cheng, and C. Xue, "Study of strain evolution mechanism in $Ge_{1-x}Sn_x$ materials grown by low temperature molecular beam epitaxy," J. Cryst. Growth **577**, 126399 (2022).
15. N. Wang, C. Xue, F. Wan, Y. Zhao, G. Xu, Z. Liu, J. Zheng, Y. Zuo, B. Cheng, and Q. Wang, "Spontaneously conversion from film to high crystalline quality stripe during molecular beam epitaxy for high Sn content GeSn," Sci. Rep. **10**, 6161 (2020).
16. S. Su, B. Cheng, C. Xue, W. Wang, Q. Cao, H. Xue, W. Hu, G. Zhang, Y. Zuo, and Q. Wang, "GeSn p-i-n photodetector for all telecommunication bands detection," Opt. Express **19**, 6400–6405 (2011).
17. A. Gassenq, F. Gencarelli, J. Van Campenhout, Y. Shimura, R. Loo, G. Narcy, B. Vincent, and G. Roelkens, "GeSn/Ge heterostructure short-wave infrared photodetectors on silicon," Opt. Express **20**, 27297–27303 (2012).
18. W. Du, T. Pham, J. Margetis, H. Tran, S. A. Ghetmiri, A. Mosleh, G. Sun, R. A. Soref, J. Tolle, H. A. Naseem, B. Li, and S.-Q. Yu, "Si based mid-infrared GeSn photodetectors and light emitters," Proc. SPIE **9555**, 95550E (2015).
19. T. Pham, W. Du, H. Tran, J. Margetis, J. Tolle, G. Sun, R. A. Soref, H. A. Naseem, B. Li, and S. Q. Yu, "Systematic study of Si-based GeSn photodiodes with 2.6 μm detector cutoff for short-wave infrared detection," Opt. Express **24**, 4519–4531 (2016).
20. W. Du, S. Ghetmiri, S. Al-Kabi, A. Mosleh, P. Thach, Y. Zhou, H. Tran, G. Sun, R. Soref, J. Margetis, J. Tolle, B. Li, M. Mortazavi, H. Naseem, and S.-Q. Yu, "Silicon-based $Ge_{0.89}Sn_{0.11}$ photodetector and light emitter towards mid-infrared applications," Proc. SPIE **10108**, 1010813 (2017).
21. H. Tran, T. Pham, J. Margetis, Y. Zhou, W. Dou, P. C. Grant, J. M. Grant, S. Al-Kabi, G. Sun, R. A. Soref, J. Tolle, Y.-H. Zhang, W. Du, B. Li, M. Mortazavi, and S.-Q. Yu, "Si-based GeSn photodetectors toward mid-infrared imaging applications," ACS Photon. **6**, 2807–2815 (2019).
22. M. R. M. Atalla, S. Assali, A. Attiaoui, C. Lemieux-Leduc, A. Kumar, S. Abdi, and O. Moutanabbir, "All-group IV transferable membrane mid-infrared photodetectors," Adv. Funct. Mater. **31**, 2006329 (2020).
23. J. Rathore, A. Nanwani, S. Mukherjee, S. Das, O. Moutanabbir, and S. Mahapatra, "Composition uniformity and large degree of strain relaxation in MBE-grown thick GeSn epitaxial layers, containing 16% Sn," J. Phys. D **54**, 185105 (2021).
24. J. Zheng, W. Huang, Z. Liu, C. Xue, C. Li, Y. Zuo, B. Cheng, and Q. Wang, "Influence of H_2 on strain evolution of high-Sn-content $Ge_{1-x}Sn_x$ alloys," J. Mater. Sci. **52**, 431–436 (2016).
25. J. Zheng, Z. Liu, Y. Zhang, Y. Zuo, C. Li, C. Xue, B. Cheng, and Q. Wang, "Growth of high-Sn content (28%) GeSn alloy films by sputtering epitaxy," J. Cryst. Growth **492**, 29–34 (2018).
26. I. Dascalescu, N. C. Zoita, A. Slav, E. Matei, S. Iftimie, F. Comanescu, A. M. Lepadatu, C. Palade, S. Lazanu, D. Buca, V. S. Teodorescu, M. L. Ciurea, M. Braic, and T. Stoica, "Epitaxial GeSn obtained by high power impulse magnetron sputtering and the heterojunction with embedded GeSn nanocrystals for shortwave infrared detection," ACS Appl. Mater. Interfaces **12**, 33879–33886 (2020).
27. W. Dou, Y. Zhou, J. Margetis, S. A. Ghetmiri, S. Al-Kabi, W. Du, J. Liu, G. Sun, R. A. Soref, J. Tolle, B. Li, M. Mortazavi, and S. Q. Yu,

"Optically pumped lasing at 3 μm from compositionally graded GeSn with tin up to 22.3," Opt. Lett. **43**, 4558–4561 (2018).
28. Y. Zhou, W. Dou, W. Du, S. Ojo, H. Tran, S. A. Ghetmiri, J. Liu, G. Sun, R. Soref, J. Margetis, J. Tolle, B. Li, Z. Chen, M. Mortazavi, and S.-Q. Yu, "Optically pumped GeSn lasers operating at 270 K with broad waveguide structures on Si," ACS Photon. **6**, 1434–1441 (2019).
29. Y. Zhou, Y. Miao, S. Ojo, H. Tran, G. Abernathy, J. M. Grant, S. Amoah, G. Salamo, W. Du, J. Liu, J. Margetis, J. Tolle, Y.-H. Zhang, G. Sun, R. A. Soref, B. Li, and S.-Q. Yu, "Electrically injected GeSn lasers on Si operating up to 100 K," Optica **7**, 924–928 (2020).
30. X. Liu, J. Zheng, M. Li, F. Wan, C. Niu, Z. Liu, Y. Zuo, C. Xue, and B. Cheng, "Growth of relaxed GeSn film with high Sn content via Sn component-grade buffer layer structure," J. Phys. D **54**, 435101 (2021).
31. C. Xu, P. M. Wallace, D. A. Ringwala, S. L. Y. Chang, C. D. Poweleit, J. Kouvetakis, and J. Menéndez, "Mid-infrared (3–8 μm) $Ge_{1-y}Sn_y$ alloys ($0.15 < y < 0.30$): synthesis, structural, and optical properties," Appl. Phys. Lett. **114**, 212104 (2019).
32. H. H. Tseng, K. Y. Wu, H. Li, V. Mashanov, H. H. Cheng, G. Sun, and R. A. Soref, "Mid-infrared electroluminescence from a $Ge/Ge_{0.922}Sn_{0.078}/Ge$ double heterostructure p-i-n diode on a Si substrate," Appl. Phys. Lett. **102**, 182106 (2013).
33. W. Yu, S. Li, Y. Zhang, W. Ma, T. Sun, J. Yuan, K. Fu, and Q. Bao, "Near-infrared photodetectors based on $MoTe_2$ /graphene heterostructure with high responsivity and flexibility," Small **13**, 1700268 (2017).